

# A Modified Dynamic Framework for the Atmospheric Spectral Model and Its Application

TONGWEN WU

*Beijing Climate Center, China Meteorological Administration, Beijing, China*

RUCONG YU

*China Meteorological Administration, Beijing, China*

FANG ZHANG

*Beijing Climate Center, China Meteorological Administration, Beijing, China*

(Manuscript received 14 May 2007, in final form 27 December 2007)

## ABSTRACT

This paper describes a dynamic framework for an atmospheric general circulation spectral model in which a reference stratified atmospheric temperature and a reference surface pressure are introduced into the governing equations so as to improve the calculation of the pressure gradient force and gradients of surface pressure and temperature. The vertical profile of the reference atmospheric temperature approximately corresponds to that of the U.S. midlatitude standard atmosphere within the troposphere and stratosphere, and the reference surface pressure is a function of surface terrain geopotential and is close to the observed mean surface pressure. Prognostic variables for the temperature and surface pressure are replaced by their perturbations from the prescribed references. The numerical algorithms of the explicit time difference scheme for vorticity and the semi-implicit time difference scheme for divergence, perturbation temperature, and perturbation surface pressure equation are given in detail. The modified numerical framework is implemented in the Community Atmosphere Model version 3 (CAM3) developed at the National Center for Atmospheric Research (NCAR) to test its validation and impact on simulated climate. Both the original and the modified models are run with the same spectral resolution (T42), the same physical parameterizations, and the same boundary conditions corresponding to the observed monthly mean sea surface temperature and sea ice concentration from 1971 to 2000. This permits one to evaluate the performance of the new dynamic framework compared to the commonly used one. Results show that there is a general improvement for the simulated climate at regional and global scales, especially for temperature and wind.

## 1. Introduction

In terrain-following  $\sigma$  coordinates or pressure-based terrain-following hybrid  $\eta$  coordinates, the horizontal pressure gradient force (PGF) in the momentum equations appears in the form of two large terms. One involves the gradient of pressure along a constant  $\sigma$  surface; the other, the gradient of geopotential height. Near steep topography these terms are large, comparable in magnitude, and opposite in sign. Therefore, a

small error in computing either term near steep topography can result in a large error in the total PGF.

A number of methods have been proposed to reduce the error in computing PGF in atmospheric general circulation simulation when using  $\sigma$  coordinates (e.g., Gary 1973; Janjić 1977; Arakawa and Suarez 1983; Mahrer 1984; Mesinger and Janjić 1985; Michailović and Janjić 1986; Janjić and Janjić 1993; Lin 1997, 1998; Janjić 1998). For example, Corby et al. (1972) and Simmons and Burridge (1981) developed a vertical finite difference scheme for the hydrostatic equation in which the pressure gradient is exact when the temperature is a linear function of the natural logarithm of pressure. Following Corby et al. (1972) and Simmons and Burridge (1981), Arakawa and Suarez (1983) derived a fam-

---

*Corresponding author address:* Dr. Tongwen Wu, National Climate Center, China Meteorological Administration, 46 Zhongguancun Nandajie, Beijing 100081, China.  
E-mail: twwu@cma.gov.cn

ily of numerical schemes for the atmospheric primitive equations in  $\sigma$  coordinates in which the pressure gradient is exact for certain atmospheres. Using a different approach, Gary (1973) showed that the size of the two terms in the pressure gradient in  $\sigma$  coordinates is reduced, and the truncation error therefore reduced, if a horizontally uniform reference state density field, and its associated hydrostatic pressure field, is removed before computing the individual pressure gradient terms. Gary's results were confirmed by the work of Johnson and Uccellini (1983), who found that the pressure gradient error in the case of a stratified flow over an isolated mountain was reduced by a factor of 4 when an adiabatic reference state was removed from the hydrostatic equation.

It was commonly believed that the pressure gradient force errors in  $\sigma$ -coordinate spectral models were small or unimportant (Simmons 1987). But, the work of Janjić (1989) assessed the order of magnitude of the pressure gradient force errors in  $\sigma$ -coordinate spectral models in the case of small-scale mountains and showed that the errors of the spectral method can be large and the spectral pressure gradient force errors are, in a root-mean-square sense, larger than those of the finite-difference method. Chen et al. (1987) demonstrated that the truncated spectral errors could be large enough to deform the atmospheric flow. By introducing the reference atmosphere (both temperature and geopotential height) suggested by Zeng (1963) into the adiabatic spectral model of the European Centre for Medium-Range Weather Forecasts (ECMWF) and removing it from the hydrostatic equation, Chen et al. (1987) could efficiently reduce the truncated spectral errors, Gibbs waves, and negative topography. Furthermore, Chen and Simmons (1989) also used the hydrostatic extraction of a reference atmosphere in the operational medium-range prediction model, which improved mean statistical scores for 1000–200-hPa height 10-day forecasts over the globe. This significantly improved forecasts in Southern Hemisphere (Chen and Simmons 1989; Simmons and Chen 1991). Sheng et al. (1992) introduced a modified reference atmosphere scheme [designed by Zhang et al. (1990) on the basis of the work of Zeng (1963) and Zeng et al. (1989)] into the Bureau of Meteorology Research Centre's (BMRC's) global spectral model. The 5-day forecasts demonstrate a positive effect of the hydrostatic extraction scheme, particularly at upper levels over the tropics and Antarctic region.

Apart from error in computing the PGF near steep topography, the model errors could also be caused by vertical discretization. Sundqvist (1975, 1976) distinguished between truncation errors due to horizontal differencing and vertical differencing, and showed that

the most significant errors are produced by sharp temperature inversions such as those that occur at the tropopause. In fact, the commonly used prognostic equations of atmospheric vorticity, divergence, temperature, and surface pressure for spectral atmospheric models in  $\sigma$  or hybrid  $\eta$  coordinates include four terms  $\nabla^2(\phi)$ ,  $\partial T/\partial p$ ,  $\nabla T$ , and  $\nabla(\ln p_s)$ , where  $\phi$  is geopotential height,  $T$  temperature,  $p_s$  surface pressure, and  $\nabla^2$  is the horizontal diffusion operator. These terms may have a large computing error near steep topography or at altitudes with high-order discontinuous temperature related to pressure, such as at the tropopause.

Although the advantage of introducing a "standard atmosphere" to improve weather forecast is evident [as in the above references, or in other similar works such as Wu et al. (1996), Dong et al. (2001), and Wu et al. (2003)], there is, to our knowledge, no complete work reporting the impact on long-term climate simulations.

The purpose of this work is (i) to pursue the general approach proposed in earlier works, (ii) to suggest and introduce a new particular reference atmospheric temperature and geopotential, as well as a reference surface pressure for atmospheric spectral models, so as to reduce the truncation errors caused by steep topography and vertical discretization, and (iii) to explore its validity for climate simulations.

The outline of the paper is as follows: A set of modified atmospheric governing equations for the National Center for Atmospheric Research (NCAR) Community Atmosphere Model version 3 (CAM3) are described in section 2. Section 3 gives the details of time differencing and the vertical finite difference scheme, which originate from the Eulerian dynamic core in CAM3 described by Collins et al. (2004). To evaluate its performance compared to the original dynamic, the modified spectral dynamic framework is implemented in CAM3 in place of the original Eulerian dynamic core without modifying the model physics. The dynamic-modified CAM3 is referred to as CAM3D in this work. Validation for CAM3D is presented in section 4, and section 5 is a summary and discussion.

## 2. Governing equations

In the vertical, a general pressure-based terrain-following  $\eta(p, p_s)$  coordinates (Simmons and Burridge 1981; Simmons and Strüfing 1981) for which upper-level model surfaces flatten over steep terrain is used. Usually one employs the explicit relationship between full-level or half-level pressure  $p$  and the surface pressure  $p_s$  to determine a vertical coordinate  $\eta$  implicitly; that is,

$$p(\lambda, \varphi, \eta) = A(\eta)p_0 + B(\eta)p_s(\lambda, \varphi), \quad (1)$$

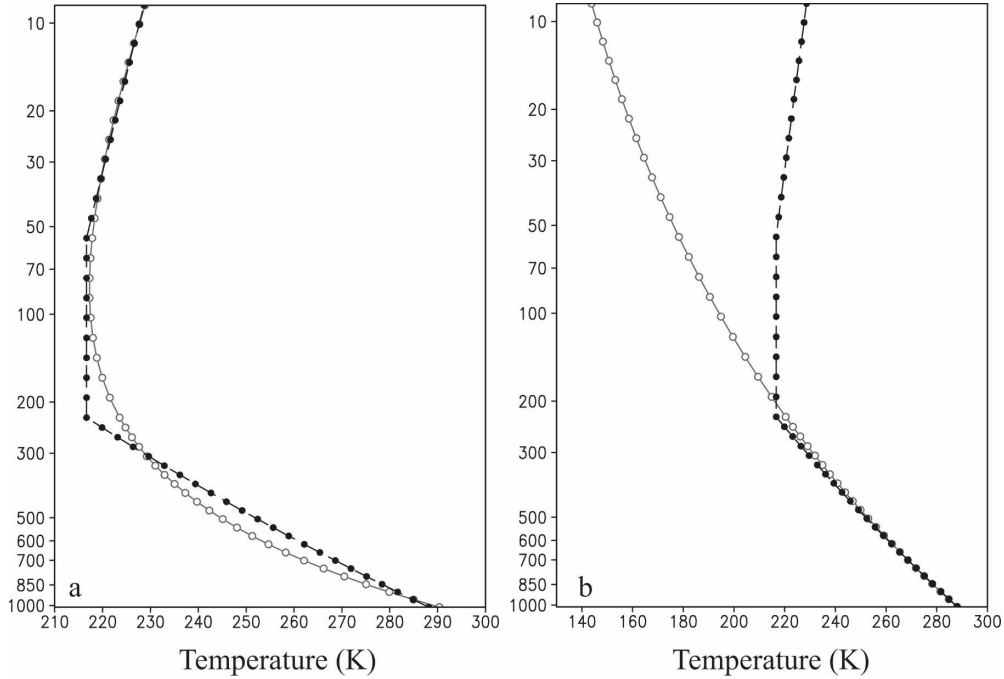


FIG. 1. The vertical profile of the reference atmospheric temperature (K) (hollow points) (a) as used in this paper and (b) as suggested by Zeng (1963) [i.e., the expression (60) in this paper], together with the U.S. midlatitude standard atmospheric temperature (solid points).

where  $p_0$  is a constant and  $A(\eta)$  and  $B(\eta)$  must be defined so that  $\eta(0, p_s) = 0$  and  $\eta(p_s, p_s) = 1$ .

The horizontal momentum equations may be written as

$$\frac{du}{dt} = fv + \frac{uv}{a} \tan\varphi - \left( \frac{RT_v}{a \cos\varphi} \frac{\partial \ln p}{\partial \lambda} + \frac{1}{a \cos\varphi} \frac{\partial \phi}{\partial \lambda} \right) + F_u + H_u \quad \text{and} \quad (2)$$

$$\frac{dv}{dt} = -fu - \frac{uv}{a} \tan\varphi - \left( \frac{RT_v}{a} \frac{\partial \ln p}{\partial \varphi} + \frac{1}{a} \frac{\partial \phi}{\partial \varphi} \right) + F_v + H_v, \quad (3)$$

where

$$\frac{d}{dt} = \frac{\partial}{\partial t} + u \frac{\partial}{a \cos\varphi \partial \lambda} + v \frac{\partial}{a \partial \varphi} + \eta \frac{\partial}{\partial \eta}.$$

Here  $f$  is the Coriolis parameter,  $t$  time,  $\varphi$  latitude,  $\lambda$  longitude,  $a$  the mean radius of the earth,  $R$  the gas constant for dry air;  $\eta$  the vertical velocity in  $\eta$  coordinates;  $u$  and  $v$  are the zonal and meridional wind components respectively, and  $\phi$  the geopotential height;  $T_v$  is the virtual temperature, given by  $T_v = [1 + (R_v/R - 1)q]T$ , where  $T$  is temperature,  $q$  specific humidity, and  $R_v$  the gas constant for water vapor. Terms  $H$  and  $F$  represent the sources and sinks due to horizontal and vertical diffusion of momentum, respectively.

We define a stratified reference atmospheric temperature  $\bar{T}(p)$ , which is derived from the vertical profile of U.S. midlatitude standard atmospheric temperature using a nonlinear regression as follows:

$$\bar{T}(p) \equiv p(a_T + b_T e^{c_T \ln p}), \quad (4)$$

where  $a_T = 0.09923 \text{ K mb}^{-1}$ ,  $b_T = 247.7874 \text{ K mb}^{-1}$ , and  $c_T = -1.0385$ . As shown in Fig. 1a, the vertical profile  $\bar{T}(p)$  is close to that of the U.S. midlatitude standard atmosphere.

Now, a reference atmospheric geopotential height  $\bar{\phi}(p)$  can be deduced as

$$\bar{\phi}(p) \equiv -R \left[ a_T(p - p_{s0}) + \frac{b_T}{(1 + c_T)} e^{(1+c_T) \ln(p/p_{s0})} \right], \quad (5)$$

where  $p_{s0}$  is constant and may be set to 1013 hPa. It is clear that the hydrostatic balance holds:

$$\frac{\partial \bar{\phi}}{\partial \ln p} = -R\bar{T}. \quad (6)$$

The  $\phi$ ,  $T$ , and  $T_v$  perturbations from  $\bar{T}(p)$  or  $\bar{\phi}(p)$  are defined as follows:

$$T_v(\lambda, \varphi, \eta) \equiv \bar{T}(p) + T'_v(\lambda, \varphi, \eta), \quad (7)$$

$$T(\lambda, \varphi, \eta) \equiv \bar{T}(p) + T'(\lambda, \varphi, \eta), \quad \text{and} \quad (8)$$

$$\phi(\lambda, \varphi, \eta) \equiv \bar{\phi}(p) + \phi'(\lambda, \varphi, \eta). \quad (9)$$

The hydrostatic equation is

$$\frac{\partial \phi}{\partial \ln p} = -RT'_v \tag{10}$$

Thus, the pressure gradient force in the momentum equations (2) and (3) can be rewritten as

$$\frac{1}{a \cos \varphi} \left[ \frac{\partial \phi}{\partial \lambda} + RT'_v \frac{\partial \ln(p)}{\partial \lambda} \right] = \frac{1}{a \cos \varphi} \times \left[ \frac{\partial \phi'}{\partial \lambda} + RT'_v \frac{\partial \ln(p)}{\partial \lambda} \right], \text{ and} \tag{11}$$

$$\frac{1}{a} \left[ \frac{\partial \phi}{\partial \varphi} + RT'_v \frac{\partial \ln(p)}{\partial \varphi} \right] = \frac{1}{a} \left[ \frac{\partial \phi'}{\partial \varphi} + RT'_v \frac{\partial \ln(p)}{\partial \varphi} \right]. \tag{12}$$

It is clear that the size of the two terms in the PGF and the truncation error could be decreased using the expression on the rhs of Eqs. (11) and (12). The momentum Eqs. (2) and (3) may be rewritten as

$$\frac{du}{dt} = f v + \frac{uv}{a} \tan \varphi - \left[ \frac{RT'_v}{a \cos \varphi} \frac{\partial \ln(p)}{\partial \lambda} + \frac{1}{a \cos \varphi} \frac{\partial \phi'}{\partial \lambda} \right] + F_u + H_u \text{ and} \tag{13}$$

$$\frac{dv}{dt} = -f u - \frac{uv}{a} \tan \varphi - \left[ \frac{RT'_v}{a} \frac{\partial \ln(p)}{\partial \varphi} + \frac{1}{a} \frac{\partial \phi'}{\partial \varphi} \right] + F_v + H_v. \tag{14}$$

To apply the spectral method, the prognostic equations for horizontal winds are commonly replaced by those of relative vorticity  $\zeta$  and divergence  $D$ . Thus,

$$\frac{\partial \zeta}{\partial t} = \frac{1}{a(1-\mu^2)} \frac{\partial(P_v)}{\partial \lambda} - \frac{1}{a} \frac{\partial(P_u)}{\partial \mu} + H_\zeta \text{ and} \tag{15}$$

$$\frac{\partial D}{\partial t} = \frac{1}{a(1-\mu^2)} \frac{\partial(P_u)}{\partial \lambda} + \frac{1}{a} \frac{\partial(P_v)}{\partial \mu} - \nabla^2(E + \phi') + H_D, \tag{16}$$

where

$$\zeta = \frac{1}{a \cos \varphi} \left[ \frac{\partial v}{\partial \lambda} - \frac{\partial}{\partial \varphi} (u \cos \varphi) \right],$$

$$D = \frac{1}{a \cos \varphi} \left[ \frac{\partial u}{\partial \lambda} + \frac{\partial}{\partial \varphi} (v \cos \varphi) \right],$$

$$P_u = (\zeta + f)V - \dot{\eta} \frac{\partial p}{\partial \eta} \frac{\partial U}{\partial p} - R \frac{T'_v}{a} \frac{\partial \ln(p)}{\partial \lambda} + F_u,$$

$$P_v = -(\zeta + f)U - \dot{\eta} \frac{\partial p}{\partial \eta} \frac{\partial V}{\partial p} - R \frac{T'_v \cos \varphi}{a} \frac{\partial \ln(p)}{\partial \varphi}$$

$$+ F_v,$$

$$\mu \equiv \sin(\varphi),$$

$$(U, V) \equiv (u, v) \cos(\varphi),$$

and

$$E = u^2 + v^2.$$

The spherical horizontal Laplacian operator  $\nabla^2$  is denoted by

$$\nabla^2 = \frac{1}{a^2 \cos^2 \varphi} \left[ \frac{\partial^2}{\partial \lambda^2} + \cos \varphi \frac{\partial}{\partial \varphi} \left( \cos \varphi \frac{\partial}{\partial \varphi} \right) \right]. \tag{17}$$

When the streamfunction  $\psi$  and velocity potential  $\chi$  are introduced,

$$U = \frac{1}{a} \frac{\partial \chi}{\partial \lambda} - \frac{(1-\mu^2)}{a} \frac{\partial \psi}{\partial \mu} \tag{18}$$

$$V = \frac{1}{a} \frac{\partial \psi}{\partial \lambda} + \frac{(1-\mu^2)}{a} \frac{\partial \chi}{\partial \mu}, \tag{19}$$

where  $\psi$  and  $\chi$  are, respectively,

$$\zeta = \nabla^2 \psi, \text{ and} \tag{20}$$

$$D = \nabla^2 \chi. \tag{21}$$

With the aid of Eqs. (6), (7), (9) and (10), the perturbation geopotential  $\phi'$  is determined by

$$\frac{\partial \phi'}{\partial \ln p} = -RT'_v. \tag{22}$$

This means that there exists a hydrostatic balance between  $\phi'$  and  $T'_v$ .

The thermodynamic equation may be written as

$$\frac{dT}{dt} = \frac{R}{c_p^*} T_v \frac{\omega}{p} + Q + H_T + F_T, \tag{23}$$

where  $Q$  represents the sources and sinks from the parameterization for temperature including the radiative and convective heating,  $H_T$  and  $F_T$  represent the horizontal and vertical diffusion of temperature, and  $\omega$  is the pressure vertical velocity. On the assumption in Eq. (8), we have

$$\frac{dT}{dt} = \frac{d\bar{T}(p)}{dt} + \frac{dT'}{dt} = \frac{d\bar{T}(p)}{dp} \omega + \frac{dT'}{dt}, \tag{24}$$

so the prognostic equation of perturbation  $T'$  may be deduced as

$$\begin{aligned} \frac{\partial T'}{\partial t} = & -\frac{1}{a \cos^2 \varphi} \left[ \frac{\partial(T'U)}{\partial \lambda} + (1-\mu^2) \frac{\partial(T'V)}{\partial \mu} \right] + T'D \\ & - \dot{\eta} \frac{\partial p}{\partial \eta} \frac{\partial T'}{\partial p} + \frac{R}{c_p^*} T_v \frac{\omega}{p} - \frac{\partial \bar{T}}{\partial p} \omega + Q + F_T + H_T. \end{aligned} \tag{25}$$

The continuity equation in  $\eta$  coordinates is given by

$$\frac{\partial}{\partial \eta} \left( \frac{\partial p}{\partial t} \right) + \nabla \cdot \left( \mathbf{V} \frac{\partial p}{\partial \eta} \right) + \frac{\partial}{\partial \eta} \left( \dot{\eta} \frac{\partial p}{\partial \eta} \right) = 0, \tag{26}$$

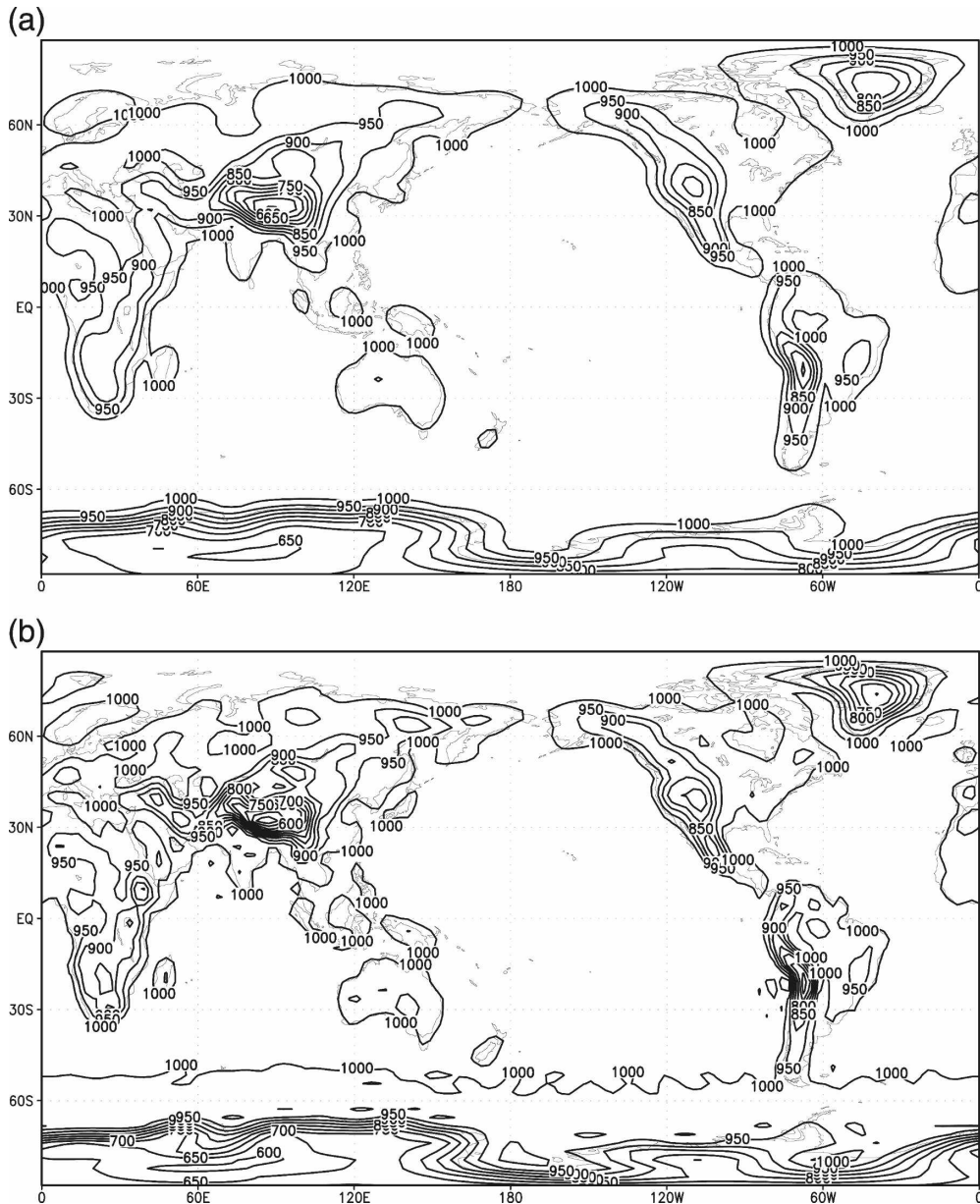


FIG. 2. Global distribution of the (top) reference surface pressure  $\bar{p}_s$  and (bottom) annual mean surface pressure for the 1971–2000 NCEP reanalyses. Contour increment is 50 hPa.

where  $\mathbf{V} = (u, v)$  the vertical velocity  $\dot{\eta}$  is computed from

$$\dot{\eta} \frac{\partial p}{\partial \eta} = - \frac{\partial p}{\partial t} - \int_{(\eta_t)}^{(\eta)} \left( \nabla \cdot \mathbf{V} \frac{\partial p}{\partial \eta} \right) d\eta, \quad (27)$$

with the boundary conditions  $\dot{\eta} = 0$  at  $\eta = \eta_t$ , the top level of the model. Then the surface pressure  $p_s$  tendency may be deduced as

$$\frac{\partial p_s}{\partial t} = - \int_{(\eta_t)}^{(\eta)} \left( \nabla \cdot \mathbf{V} \frac{\partial p}{\partial \eta} \right) d\eta, \quad (28)$$

and the pressure vertical velocity  $\omega$  is given by

$$\omega = \mathbf{V} \nabla p - \int_{(\eta_t)}^{(\eta)} \left( \nabla \cdot \mathbf{V} \frac{\partial p}{\partial \eta} \right) d\eta. \quad (29)$$

In practice, the prognostic solutions may present excessive noises caused by  $\partial p_s / \partial t$  and  $\nabla p_s$ . The prognostic equations including  $\partial p_s / \partial t$ ,  $p_s$ , and  $\nabla p_s$  are commonly replaced by those for  $\partial \ln p_s / \partial t$ ,  $\ln p_s$ , and  $\nabla(\ln p_s)$  (e.g., Roeckner et al. 2003; Collins et al. 2004). To reduce the

truncation error of  $\nabla(\ln p_s)$ , especially near steep topography, we introduce a reference surface pressure  $\bar{p}_s$  so that

$$\bar{\Pi} \equiv \ln(\bar{p}_s) = -\frac{\phi_s}{RT_{s0}} + \ln(\bar{p}_{s0}), \quad (30)$$

where  $\phi_s$  is the model surface geopotential,  $\bar{T}_{s0}$  a constant (273 K in this work), and  $\bar{p}_{s0}$  a reference sea level pressure (1000 hPa). As shown in Fig. 2, the pattern of global distribution of  $\bar{p}_s$  resembles that of the observed annual mean surface pressure from the 1961–2000 National Centers for Environmental Prediction (NCEP) reanalyses.

Now, we define the perturbation surface pressure  $\Pi'$  as

$$\Pi(\lambda, \varphi) \equiv \bar{\Pi}(\lambda, \varphi) + \Pi'(\lambda, \varphi), \quad (31)$$

where  $\Pi \equiv \ln(p_s)$ . Then the prognostic equation (28) for surface pressure is rewritten as

$$\frac{\partial \Pi'}{\partial t} = -\int_{(\eta)}^{(1)} \mathbf{V} \cdot \nabla(\bar{\Pi} + \Pi') d\left(\frac{\partial p}{\partial p_s}\right) - \frac{1}{p_s} \int_{p(\eta)}^{p(1)} Ddp. \quad (32)$$

Thus, the vertical velocity  $\omega$  in pressure coordinates and  $\dot{\eta}$  in hybrid coordinates are rewritten as

$$\omega = \frac{\partial p}{\partial p_s} p_s \mathbf{V} \cdot \nabla(\bar{\Pi} + \Pi') - \int_{(\eta)}^{(\eta)} p_s \mathbf{V} \cdot \nabla(\bar{\Pi} + \Pi') d\left(\frac{\partial p}{\partial p_s}\right) - \int_{p(\eta)}^{p(\eta)} Ddp \quad (33)$$

$$\dot{\eta} \frac{\partial p}{\partial \eta} = \frac{\partial p}{\partial p_s} \left[ \int_{(\eta)}^{(1)} p_s \mathbf{V} \cdot \nabla(\bar{\Pi} + \Pi') d\left(\frac{\partial p}{\partial p_s}\right) + \int_{p(\eta)}^{p(1)} Ddp \right] - \left[ \int_{(\eta)}^{(\eta)} p_s \mathbf{V} \cdot \nabla(\bar{\Pi} + \Pi') d\left(\frac{\partial p}{\partial p_s}\right) + \int_{p(\eta)}^{p(\eta)} Ddp \right], \quad (34)$$

where  $\nabla \bar{\Pi}$  is a large term relative to  $\nabla \Pi'$  and does not change with time.

To complete the governing equation, we recall that the prognostic equation for specific humidity  $q$  is unchanged and may be written as

$$\frac{dq}{dt} = S, \quad (35)$$

where  $S$  denotes the source and sink of moisture including convective condensation and diffusion of water vapor.

### 3. The time differencing scheme

A semi-implicit time scheme is used for the divergence equation (16), the perturbation temperature equation (25), and the perturbation surface pressure equation (32), and an explicit time integration scheme is used for the vorticity equation (15). The linear parts of those terms related to gravitational waves are treated implicitly and the remaining nonlinear parts are treated explicitly. To linearize the gravitational wave terms, a reference state for temperature  $T^r(\eta)$  and pressure  $p^r(\eta)$  is introduced. For simplification,  $T^r(\eta)$  is set to 300 K for all  $\eta$ , and  $p^r(\eta) = A(\eta)p_0 + B(\eta)p'_s$ , in which  $p'_s = 1000$  hPa. Following the derivation given in the appendix, if there is no horizontal diffusion source, the time integrations may be written as

$$\frac{\underline{\xi}^{n+1} - \underline{\xi}^{n-1}}{2\Delta t} = \frac{1}{a(1 - \mu^2)} \frac{\partial(P'_u)^n}{\partial \lambda} - \frac{1}{a} \frac{\partial(P'_u)^n}{\partial \mu} \quad (36)$$

$$\begin{aligned} \frac{D^{n+1} - D^{n-1}}{2\Delta t} &= \frac{1}{a(1 - \mu^2)} \frac{\partial(P'_u)^n}{\partial \lambda} + \frac{1}{a} \frac{\partial(P'_u)^n}{\partial \mu} - \nabla^2[\underline{E}^n + (\underline{\phi}')^n] - R(\underline{b}^r + \underline{c}^r)\nabla^2 \left[ \frac{(\Pi')^{n-1} + (\Pi')^{n+1}}{2} - (\Pi')^n \right] \\ &\quad - R\mathbf{H}^r \nabla^2 \left[ \frac{(T')^{n-1} + (T')^{n+1}}{2} - (T')^n \right] \end{aligned} \quad (37)$$

$$\frac{(T')^{n+1} - (T')^{n-1}}{2\Delta t} = -\frac{1}{a \cos^2 \varphi} \left[ \frac{\partial(T'U)^n}{\partial \lambda} + (1 - \mu^2) \frac{\partial(T'V)^n}{\partial \mu} \right] + \underline{F}^n_{\underline{Q}} - \mathbf{K}^r \left( \frac{D^{n+1} + D^{n-1}}{2} - D^n \right), \quad (38)$$

$$\frac{(\Pi')^{n+1} - (\Pi')^{n-1}}{2\Delta t} = -\frac{1}{\pi^n} \{ (\underline{D}^n)^T \underline{\Delta p}^n + (\mathbf{V}^n)^T [\nabla \bar{\Pi} + \nabla(\Pi')^n] p'_s \underline{\Delta B} \} - \left( \frac{D^{n-1} + D^{n+1}}{2} - D^n \right) \frac{1}{\pi^r} \underline{\Delta p}^r, \quad (39)$$

where the underbar represents a column vector in the vertical direction. The vector  $\underline{b}^r$  is taken as

$$\underline{b}^r = \begin{pmatrix} T^r p_s^r \frac{\partial p^r}{\partial p_s^r} \\ p^r \frac{\partial p^r}{\partial p_s^r} \end{pmatrix}, \tag{40}$$

and vector  $\underline{c}^r$  is the vertical differencing integral of the following expression:

$$c^r = \int_{p^r(\eta)}^{p^r(1)} \left[ \frac{\partial \bar{T}(p^r)}{\partial p^r} \frac{\partial p^r}{\partial p_s^r} p_s^r \right] d \ln p^r. \tag{41}$$

So, the components  $c_{kl}^r$  of  $\underline{c}^r$  may be expressed as

$$c_{kl}^r = \sum_{l=k}^K H_{kl}^r \left[ \frac{\partial \bar{T}(p^r)}{\partial p^r} \frac{\partial p^r}{\partial p_s^r} p_s^r \right]_l, \tag{42}$$

where  $K$  is the total vertical model layers numbered from top to bottom, and

$$H_{kl}^r = \begin{cases} \Delta p_l^r / p_l^r, & l > k, \\ \Delta p_l^r / (2p_l^r), & l = k, \\ 0, & l < k, \text{ and} \end{cases} \tag{43}$$

in which  $\Delta p_l^r = p_{k+1/2}^r - p_{k-1/2}^r$  and  $H_{kl}^r$  are the components of matrix  $\mathbf{H}^r$ . Also,  $\mathbf{K}^r$  is a matrix with components  $K_{kl}^r$ :

$$\begin{aligned} (K^r)_{kl} &= \Delta p_l^r \left( \frac{R}{c_p} T_k^r C_{lk}^r - \frac{\partial \bar{T}}{\partial p_k^r} \right) + \frac{\Delta p_l^r}{2\Delta p_k^r} [(T_k^r - \bar{T}_k^r) \\ &\quad - (T_{k-1}^r - \bar{T}_{k-1}^r)] (\varepsilon_{kl+1} - B_{k-1/2}) \\ &\quad + \frac{\Delta p_l^r}{2\Delta p_k^r} [(T_{k+1}^r - \bar{T}_{k+1}^r) - (T_k^r - \bar{T}_k^r)] \\ &\quad \times (\varepsilon_{kl} - B_{k+1/2}), \end{aligned} \tag{44}$$

where

$$C_{kl}^r = \begin{cases} 1/p_l^r, & l > k, \\ 1/(2p_l^r), & l = k, \end{cases} \tag{45}$$

and

$$\varepsilon_{kl} = \begin{cases} 1, & l \leq k, \\ 0, & l > k. \end{cases} \tag{46}$$

In Eq. (37),

$$\phi'_k = \phi' |_{\eta=1} + R \sum_{l=1}^K H_{kl}(T'_l), \tag{47}$$

where

$$\phi' |_{\eta=1} = \phi_s(\lambda, \theta) - \bar{\phi}(p_s). \tag{48}$$

The elements of vectors  $\underline{P}_\omega^n$ ,  $\underline{P}_v^n$ ,  $\underline{E}_n$ ,  $\underline{F}_Q^n$ , and  $\omega$  at levels and  $\dot{\eta} \partial p / \partial \eta$  at half-levels above are respectively expressed as

$$\begin{aligned} (P_u)_k &= (\zeta_k + f) V_k - \frac{1}{2\Delta p_k} \left[ \left( \dot{\eta} \frac{\partial p}{\partial \eta} \right)_{k+1/2} (U_{k+1} - U_k) + \left( \dot{\eta} \frac{\partial p}{\partial \eta} \right)_{k-1/2} (U_k - U_{k-1}) \right] \\ &\quad - R(T'_v)_k \left( \frac{1}{p} \frac{\partial p}{\partial p_s} \right)_k p_s \frac{1}{a} \left( \frac{\partial \bar{\Pi}}{\partial \lambda} + \frac{\partial \Pi'}{\partial \lambda} \right) + (F_U)_k, \end{aligned} \tag{49}$$

$$\begin{aligned} (P_v)_k &= -(\zeta_k + f) U_k - \frac{1}{2\Delta p_k} \left[ \left( \dot{\eta} \frac{\partial p}{\partial \eta} \right)_{k+1/2} (V_{k+1} - V_k) + \left( \dot{\eta} \frac{\partial p}{\partial \eta} \right)_{k-1/2} (V_k - V_{k-1}) \right] \\ &\quad - R(T'_v)_k \left( \frac{1}{p} \frac{\partial p}{\partial p_s} \right)_k p_s \frac{\cos \varphi}{a} \left( \frac{\partial \bar{\Pi}}{\partial \varphi} + \frac{\partial \Pi'}{\partial \varphi} \right) + (F_V)_k, \end{aligned} \tag{50}$$

$$E_k = (u_k)^2 + (v_k)^2, \tag{51}$$

$$(F_Q)_k = \left( T'D + \frac{R}{c_p^*} T_v \frac{\omega}{p} - \frac{\partial \bar{T}}{\partial p} \omega + Q + F_T \right)_k - \left[ \left( \dot{\eta} \frac{\partial p}{\partial \eta} \frac{\partial T'}{\partial p} \right)_{k+1/2} + \left( \dot{\eta} \frac{\partial p}{\partial \eta} \frac{\partial T'}{\partial p} \right)_{k-1/2} \right] / 2, \tag{52}$$

$$\left( \frac{\omega}{p} \right)_k = \left( \frac{1}{p} \frac{\partial p}{\partial p_s} \right)_k \mathbf{v}_k \cdot p_s (\nabla \bar{\Pi} + \nabla \Pi') - \sum_{l=1}^k C_{kl} [D_l \Delta p_l + \mathbf{v}_l \cdot p_s (\nabla \bar{\Pi} + \nabla \Pi') \Delta B_l], \tag{53}$$

and

$$\left( \dot{\eta} \frac{\partial p}{\partial \eta} \right)_{k+1/2} = B_{K+1/2} \sum_{l=1}^K [D_l \Delta p_l + \mathbf{v}_l \cdot p_s (\nabla \bar{\Pi} + \nabla \Pi') \Delta B_l] - \sum_{l=1}^k [D_l \Delta p_l + \mathbf{v}_l \cdot p_s (\nabla \bar{\Pi} + \nabla \Pi') \Delta B_l]. \tag{54}$$

Following the description by Collins et al. (2004), when the model dynamic includes horizontal diffusion processes, the prognostic equations are given by

$$\frac{\partial \Psi}{\partial t} = \text{dyn}(\Psi) - (-1)^i K^{(2i)} \nabla_{\eta}^{2i} \Psi \quad (55)$$

for  $\zeta$  and  $D$  and

$$\begin{aligned} \frac{\partial T'}{\partial t} = & \text{dyn}(T') - (-1)^i K^{(2i)} \left\{ \nabla_{\eta}^{2i}(T') - p_s \frac{\partial T'}{\partial p} \frac{\partial p}{\partial p_s} \right. \\ & \left. \times [\nabla_{\eta}^{2i} \bar{\Pi} + \nabla_{\eta}^{2i}(\Pi')] \right\} \quad (56) \end{aligned}$$

for  $T'$  (but  $T$  in CAM3), where  $i = 1$  or  $2$ . The notation  $\text{dyn}$  for  $\zeta$ ,  $D$ , and  $T'$  represents the finite difference in (36)–(38), respectively. The time-split forms of Eqs. (55) and (56) are identical to those in CAM3 [Eqs. (2.85)–(3.92) in Collins et al. (2004)] and are thus omitted.

In summary, our modified Eulerian dynamic core differs from the original one of CAM3 in terms of the prognostic equations for vorticity, divergence, temperature, and surface pressure. The rest of the CAM3 model, however, is unchanged, as described in Collins et al. (2004): the spectral transform method for treating the dry dynamics, the harmonic  $\nabla^2$  horizontal diffusion operator (top three model levels), the biharmonic  $\nabla^4$  horizontal diffusion operator (other model levels), the semi-Lagrangian advection transport scheme for water vapor as well as tracers, the recursive time filter, and the three-time-level “process split” coupling manner including dynamical process and physical parameterization.

#### 4. Performance of the modified dynamic core in climate simulations

CAM3 and CAM3D have the same model physics (cf. Collins et al. 2004) but different Eulerian dynamical cores. The 31-yr simulations of CAM3 and CAM3D at T42 resolution with the forcing of 1970–2000 monthly-mean global Hadley Centre Sea Ice and Sea Surface Temperature (HadISST) (Rayner et al. 2003) are performed for comparison with observations. The modified dynamics may directly cause variations of temperature and wind that influence the atmospheric circulation and even the transport of water vapor. Thus, climate fields such as the vertical structure of temperature, specific humidity, and zonal wind averaged for the last 30 years are inspected to evaluate the performance of the modified dynamical core. The primary source of validation data is the 40-yr ECMWF Re-Analysis (ERA-40) archive (see <http://www.ecmwf.int/publications> and

<http://www.ecmwf.int/research/era>). In particular, we use of the monthly-mean ERA-40 data available for the same period of model simulations (1971–2000). Seasonal-mean climatologies were regridded to T42 spectral resolution for comparison to the model-generated, pressure-interpolated fields.

##### a. Vertical profile of temperature

Figures 3a,b and 3c,d show the seasonal December–February (DJF) and June–August (JJA) zonal averages of temperature differences between CAM3 and ERA-40 and the differences between CAM3D and CAM3 for the period of 1971–2000. Overall, both CAM3 and CAM3D do a relatively good job of reproducing the analyzed thermal structure of the atmosphere. There are similar vertical structures of simulation biases in CAM3 and CAM3D (omitted). Almost all tropospheric temperatures are colder than the reanalyses. The CAM3 simulated temperatures are within 1–3 K cold bias relative to ERA-40 reanalyses for most of the domain equatorward of 50°N and 50°S below 70 hPa, except for a weak warm bias in the low to middle portion of the tropical troposphere in both hemispheres during DJF and only limited in the Northern Hemisphere (NH) during JJA. Larger cold biases produced by CAM3 and CAM3D are all near the tropopause. The maximum cold bias from CAM3 is near 200 hPa southward of 60°S and northward of 60°N, with the coldest bias near the South Pole of 15 K during DJF and 6–9 K during JJA and near the North Pole of 6 K during DJF and 10–12 K during JJA.

During the period of 1971–2000, the averaged temperature bias in CAM3 is slightly reduced in CAM3D (Figs. 3b and 3d). This is particularly true in the first 10-yr period of 1971–80 (not shown). During DJF, as shown in Fig. 3b, the positive temperature difference with respect to CAM3 covers a large region spanning the high-latitude upper troposphere and the stratosphere, especially above 250 hPa in both the hemispheres. The temperature climatology from CAM3D is greater than that from CAM3 by 0.2–0.6 K for the period 1971–2000 and the negative temperature difference covers the middle and lower troposphere below 250 hPa in the tropics and subtropics of both the hemispheres where the simulated temperature climatology in CAM3D is slightly colder than that in CAM3 by 0.2–0.4 K. The warm biases in the polar lower troposphere in both hemispheres for CAM3 (Fig. 3a) are reduced by 0.2–0.8 K in CAM3D, and the warm biases in the tropical and midlatitude stratosphere are also slightly weakened in CAM3D (Fig. 3b). The area where the improvement of simulated temperature has high statistical significance at a level of 90% or greater is

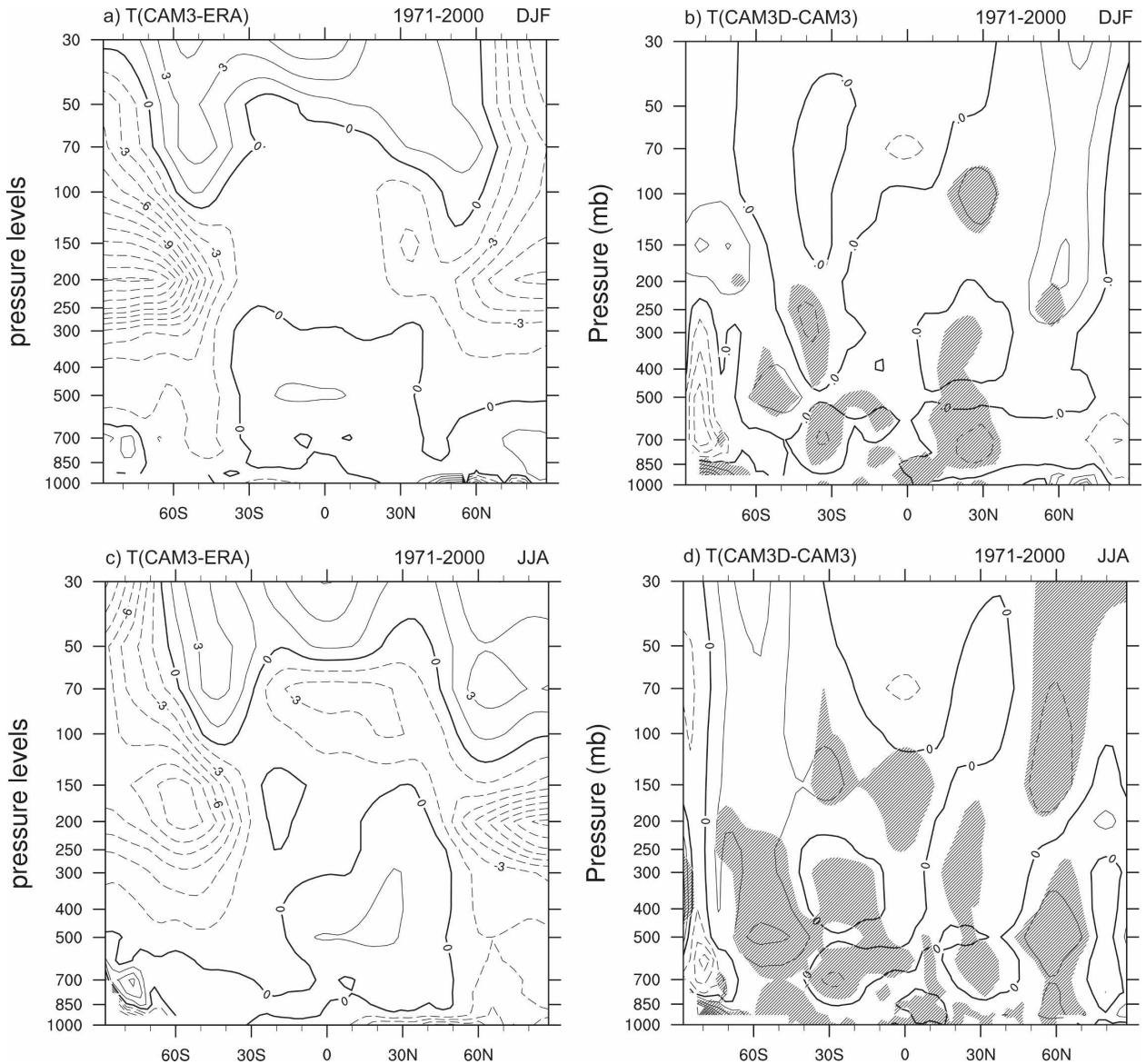


FIG. 3. Zonal-mean temperature differences between CAM3 and ERA-40 for (a) DJF and (c) JJA and between CAM3D and CAM3 for (b) DJF and (d) JJA, averaged for 1971–2000. Intervals are 1.5 K in (a) and (c) and 0.2 K in (b) and (d); dashed lines denote negative values. Shaded areas in (b) and (d) indicate where the *t* test is significant at the 90% level.

distributed mainly in the middle and lower troposphere of both hemispheres.

Improvement in temperature also occurs in boreal summer. As shown in Fig. 3d, the positive temperature differences between CAM3D and CAM3, with 0.4–0.6 K in the middle and upper troposphere and stratosphere poleward of 40°S and 0.2–0.4 K in the middle and lower troposphere north of 40°N, imply that the cold biases in CAM3 in contrast to ERA climatology (Fig. 3c) are reduced. The simulated warm biases over the northern subtropical troposphere and the high-latitude and tropical stratosphere by CAM3 are slightly

improved by the negative temperature differences between CAM3D and CAM3. Poleward of 70°S, the warm temperature bias over the lower troposphere in CAM3 is also reduced in CAM3D, and there is a negative temperature difference of about 1 K.

Although the cold bias in the tropopause in CAM3 is reduced in CAM3D, it is still remarkable in CAM3D. This large systematic error may be partly related to an improper treatment of the interaction between the troposphere and stratosphere. As shown in Figs. 3a and 3c, the stratospheric temperatures above 70 hPa are warmer than the reanalyses. The difficulty in properly

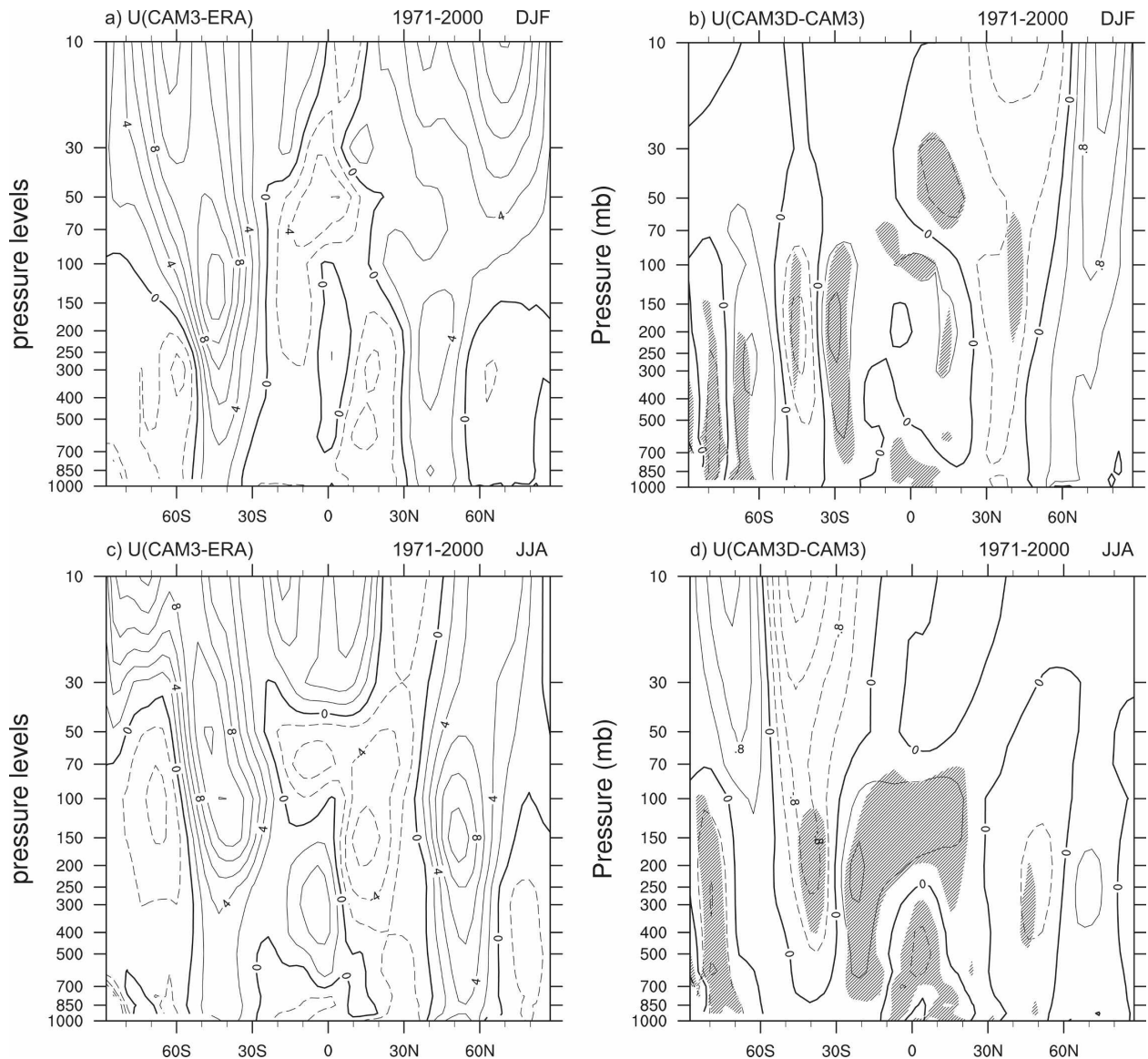


FIG. 4. As in Fig. 3 but for zonally averaged DJF and JJA mean zonal wind differences. Intervals are  $2 \text{ m s}^{-1}$  in (a) and (c) and  $0.4 \text{ m s}^{-1}$  in (b) and (d).

simulating polar tropopause temperature still remains a long-standing documented problem for many AGCMs (Boer et al. 1992).

#### b. Vertical structure of the zonal wind

The large-scale wind is closely linked to the temperature and pressure structures in the atmosphere. The zonal wind has traditionally been one of the fundamental climate variables. Figures 4a and 4c show the DJF and JJA zonal average differences of zonal winds for the period 1971–2000 in CAM3 from the ERA-40 reanalysis climatology. Overall, the zonal wind vertical structure is well simulated by both CAM3 and CAM3D.

During DJF, as shown in Fig. 4a, the zonally averaged westerlies in middle latitudes of both hemispheres between  $35^\circ$  and  $55^\circ$  latitude in CAM3 are stronger than the reanalyses by a few meters per second, with a larger westerly bias evidently over the Southern Hemisphere (SH). Poleward from  $55^\circ$  latitude there are slight easterly wind biases by  $2 \text{ m s}^{-1}$ . In tropical latitudes, the tropospheric easterlies are much stronger ( $2\text{--}4 \text{ m s}^{-1}$ ) than the reanalyses and larger biases occur in the northern tropics with a maximum up to  $-4 \text{ m s}^{-1}$  between 200 and 850 hPa. In the SH stratosphere above 100 hPa, the largest biases are near 50 hPa over the tropics with an easterly wind bias of  $2\text{--}4 \text{ m s}^{-1}$  and over

the middle to high latitudes with a westerly wind bias of  $8 \text{ m s}^{-1}$ . Although the simulated wind in the NH stratosphere poleward of  $40^\circ\text{N}$  has a westerly wind bias with respect to the ERA-40 reanalyses, the magnitude of the bias is clearly smaller than its counterpart in the SH stratosphere. In CAM3D, the spatial structure of zonal wind bias (omitted) resembles that in CAM3, that is, easterly bias in the tropics, westerly bias in midlatitudes, and an easterly bias poleward of  $60^\circ\text{S}$  and  $60^\circ\text{N}$ . Nevertheless, the CAM3D zonal wind biases in the troposphere are still slightly reduced with respect to those in CAM3. As shown in Fig. 4b, which shows the difference between CAM3D and ERA40 climatology averaged for the period 1971–2000, the improvement is displayed by the easterly wind difference between CAM3D and CAM3 over  $20^\circ\text{--}50^\circ\text{N}$  and  $30^\circ\text{--}50^\circ\text{S}$ , indicates that the stronger midlatitude westerly wind in CAM3 is decreased in CAM3D, and the tropospheric westerly wind difference poleward of  $50^\circ\text{N}$  and between  $50^\circ$  and  $75^\circ\text{S}$  indicates that the polar easterly wind bias in CAM3 is also reduced in CAM3D. The small westerly wind difference in the subtropics and the easterly wind difference at the equator still show a slight improvement of the zonal wind simulation at lower latitudes in CAM3D. But southward of  $50^\circ\text{S}$  over the stratosphere above 100 hPa, the zonal wind simulation averaged for the period 1971–2000 is particularly worse in CAM3D.

During JJA, the CAM3 biases in contrast to observations are similar to those during DJF, such as biases of westerly wind in the midlatitudes, easterly wind in the tropics, and easterly wind in higher latitudes. The strongest westerly and easterly wind biases are all located in the upper troposphere above 300 hPa and the lower stratosphere below 70 hPa. In addition, the biases in the NH are obviously stronger than those during DJF. As for CAM3D, the improvement in tropospheric zonal wind is in the region  $70^\circ\text{S}\text{--}70^\circ\text{N}$  since the differences between CAM3D and CAM3 are nearly opposite in sign to those between CAM3 and ERA-40. The bias in CAM3D is slightly reduced by  $0.4\text{--}1.0 \text{ m s}^{-1}$  for the period 1971–2000. The regions where improvement of the simulated zonal wind has high statistical significance at a level of 90% or greater is still distributed mainly in the middle and lower troposphere of both hemispheres, especially in the southern subtropics. In the southern polar region, however, the zonal wind bias in CAM3D is worse than that in CAM3.

### c. Vertical structure of the specific humidity

Water vapor and temperature are the two state variables that jointly define the moist static stability of the

atmosphere. The ability of a model to properly simulate the vertical distribution of water vapor is strongly constrained by the biases in the simulated temperature structure. The improvements in temperature and wind also induce a reduction of the simulated moisture bias.

Figures 5a and 5c show the CAM3 simulated DJF and JJA zonally averaged difference of the specific humidity from the ERA-40 reanalysis climatology, respectively. During DJF, the zonally averaged biases show a simulated atmosphere that is wetter than the ERA-40 analysis throughout most of the troposphere, especially in the northern tropics and subtropics. The main exception is a dry bias in the domain of the lower troposphere below 700 hPa between  $40^\circ\text{S}$  and  $10^\circ\text{N}$ , with the maximum exceeding  $1.5 \text{ g kg}^{-1}$  near  $850 \text{ hPa}$  at  $12^\circ\text{S}$ . The vertical distribution of the global zonal-mean specific humidity bias in CAM3D from the reanalyses clearly resembles that in CAM3 (omitted). However, the improvement of the southern tropical dry bias in CAM3D is still visible from the difference with respect to CAM3 simulation (Fig. 6b) since there is a large region of increased moisture between  $40^\circ\text{S}$  and  $10^\circ\text{N}$  below 700 hPa with the maximum about  $0.1 \text{ g kg}^{-1}$  (except for a moisture decrease between 700 hPa and 800 hPa and between  $25^\circ$  and  $5^\circ\text{S}$ ). In addition, the wet bias near the surface between  $15^\circ$  and  $50^\circ\text{N}$  in CAM3 is also reduced in CAM3D.

During JJA, the southern tropical dry bias seasonally moves northward and spreads. The region of this dry bias covers the lower troposphere below 700 hPa between  $20^\circ\text{S}$  and  $60^\circ\text{N}$  with the wettest bias  $1.8 \text{ g kg}^{-1}$  near  $5^\circ\text{N}$  (Fig. 5c). However, the water vapor in the middle troposphere between 400 and 700 hPa over the northern tropics and subtropics and poleward of  $30^\circ\text{S}$  still maintains a wet bias compared to the ERA-40 reanalyses. These biases are partly reduced in CAM3D. As shown in Fig. 5d, the CAM3D simulated a positive water vapor difference over the lower troposphere below 850 hPa at the equator and in the tropics between  $10^\circ\text{S}$  and  $15^\circ\text{N}$ , in contrast to CAM3, and the negative differences near the surface in the subtropics of both hemispheres and in the middle troposphere between 400 and 600 hPa over the zone of  $10^\circ\text{--}40^\circ\text{N}$  display some improvements in CAM3D.

### d. The 200-hPa height field

The performance of CAM3D can be quantified through a skill score for climate models based on the fidelity of the climatologically averaged 200-mb height field (Williamson 1995). This method has been used to evaluate community climate models (CCMs) (Kiehl et al. 1998) and community atmosphere models (CAMs)

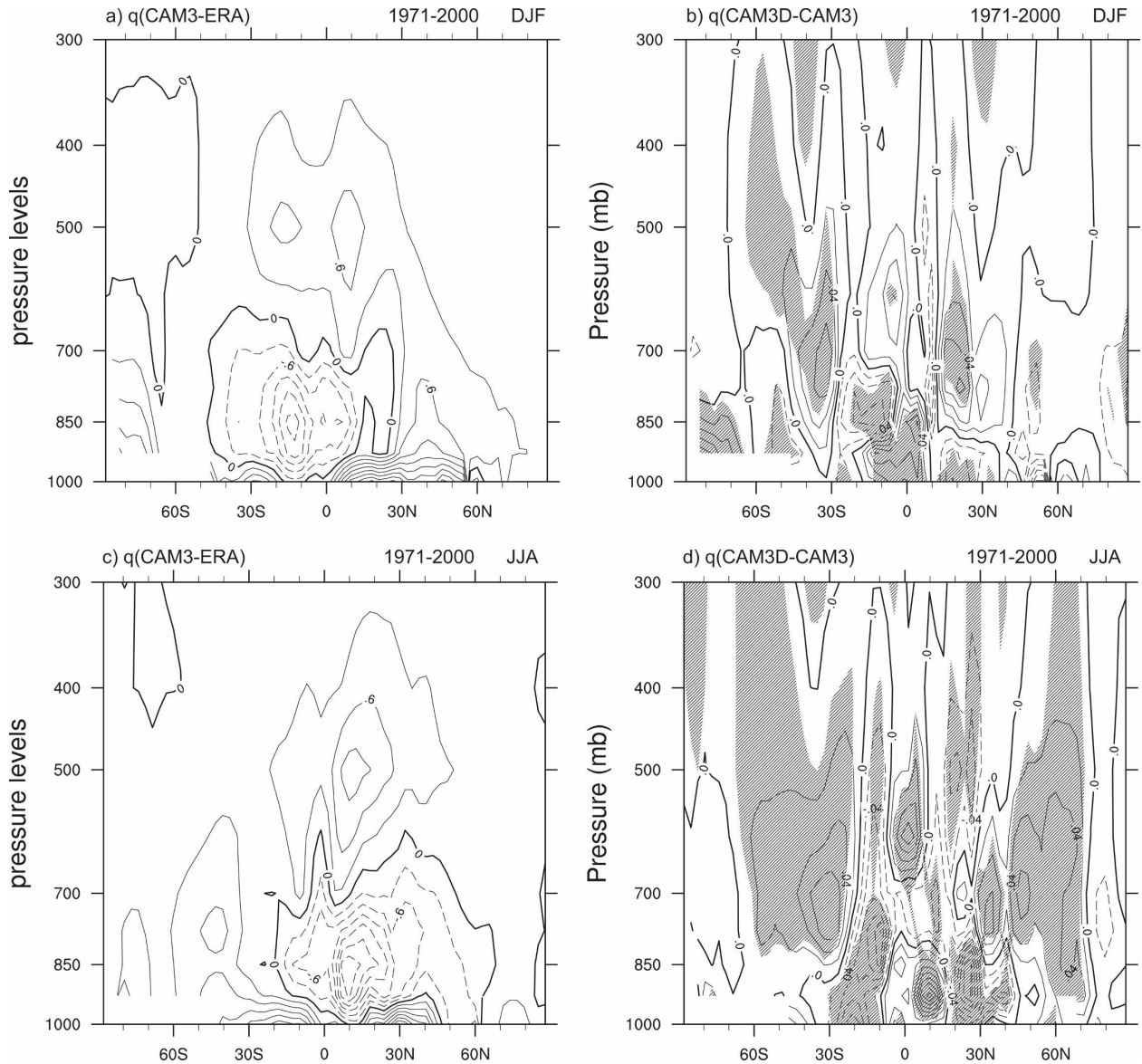


FIG. 5. As in Fig. 3 but for zonally averaged DJF and JJA mean specific humidity differences. Intervals are  $0.3 \text{ g kg}^{-1}$  in (a) and (c) and  $0.02 \text{ g kg}^{-1}$  in (b) and (d).

(Collins et al. 2006). The score is a function of the height  $z_m$  produced by the model and the height  $z_a$  from the ERA-40 reanalysis, and is given by the normalized mean square error (NMSE):

$$\text{NMSE}(z_m) = \overline{(z_m - z_a)^2} / (\overline{z_a - z_a})^2, \quad (57)$$

where an overbar denotes an area average over the domain of interest. A perfect score of 0 indicates that the model is able to reproduce the exact 200-hPa height field in the analysis. The NMSE can be rewritten as a sum of three nonnegative terms:

$$\text{NMSE}(z_m) = U(z_m) + C(z_m) + P(z_m). \quad (58)$$

As described in Kiehl et al. (1998) and Collins et al. (2006), the first term

$$U(z_m) = \left( \frac{\overline{z_m} - \overline{z_a}}{s_a} \right)^2,$$

in which  $s_m^2$  and  $s_a^2$  represent the spatial variances of the simulated and analyzed height fields, is a measure of the unconditional bias in the model and vanishes only if the average heights in the model and analysis are equal. The second term

$$C(z_m) = \left( r_{ma} - \frac{s_m}{s_a} \right)^2,$$

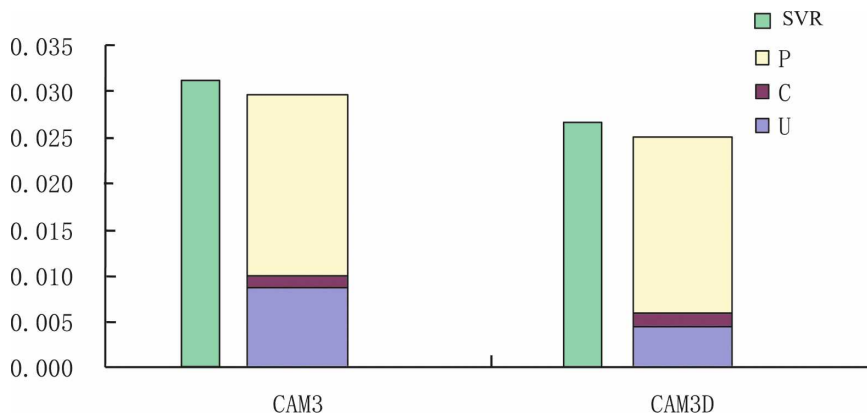


FIG. 6. NMSE and SVR for the 200-hPa height field during January of 1971–2000 in the Northern Hemisphere (30°–90°N) for CAM3 and CAM3D. For each model, the narrow lhs bar is SVR and the broad rhs bar is NMSE. The marks P, C, and U are the terms in Eq. (58) for NMSE.

in which  $r_{ma}$  is the correlation between simulations and observations, is a measure of the conditional bias in the model. It vanishes if linear regressions of the analyzed heights against the simulated heights yield slopes equal to unity. The third term  $P(z_m) = 1 - r_{ma}^2$  is a measure of the phase errors, and it vanishes if the model and analysis fields are perfectly linearly correlated.

A scaled variance ratio (SVR) is also included as a control statistic:

$$SVR(z_m) = (s_m/s_a)^2 NMSE(z_m). \quad (59)$$

It indicates whether the model variance is greater than or less than that of the observed atmosphere.

The scores SVR and NMSE, and the related terms  $U(z_m)$ ,  $C(z_m)$ , and  $P(z_m)$  for CAM3 and CAM3D, are calculated for the 200-hPa height field during January of 1971–2000 in the Northern Hemisphere (30°–90°N). The results plotted in Fig. 6 show that the simulated climate in CAM3D has been clearly improved, primarily through reduction of the unconditional error  $U(z_m)$  and then reduction of the NMSE, although CAM3D has slightly higher conditional error  $C(z_m)$  than CAM3:  $C(z_m)$  is equal to 0.00143 in CAM3D and 0.00122 in CAM3. The correlation error  $P(z_m)$  in CAM3D is slightly less than that in CAM3: it is 0.01923 in CAM3D and 0.01980 in CAM3.

Concerning the SVR, the model variance in CAM3D is also smaller than that in CAM3. The SVR is close to the NMSE for both CAM3 and CAM3D, which indicates that the NMSE is not artificially low due to damping of the model height field.

*e. The simulation in the vicinity of the Tibetan Plateau*

One of the main advantages of our modifications in CAM3D, as shown in section 2, is to reduce the error of

the pressure gradient force and then improve the horizontal circulation. Figure 7 shows the 1971–2000 averaged DJF and JJA 500-hPa zonal wind difference between the CAM3 simulation and the ERA-40 reanalyses and that between CAM3D and CAM3 simulations in the vicinity of the Tibetan Plateau, which is one of the major orographic obstacles for the atmospheric general circulation. During DJF, there is a westerly bias zone in the region of 30°–40°N, 70°–120°E with the maximum of 6 m s<sup>-1</sup> in the main body of the Tibetan Plateau and the central part of East China from CAM3, a large area of easterly biases in the lower latitudes to the south of 30°N, and two small areas of weak westerly bias to the north of 40°N from CAM3. Some of those 500-hPa zonal wind errors in CAM3 are improved in CAM3D. For example, the easterly difference between CAM3D and CAM3 covers the northwestern part of the Tibetan Plateau and the middle and eastern part of the Tibetan Plateau that spreads to East China. It indicates a decrease of the westerly bias in CAM3D in contrast to the ERA-40 data. But the easterly error over the southwestern part of the Tibetan Plateau in CAM3D seems worse than that in CAM3 (Fig. 7b). This may be attributed to the complex influence of the winter Indian monsoon and the uncertainty of the ERA-40 reanalysis data related to fewer observations at the southwestern part of the Plateau (i.e., the Himalayas).

During JJA, as shown in Figs. 7c and 7d, easterly biases of 500-hPa zonal wind in the eastern part of the Tibetan Plateau in CAM3 compared to ERA-40 climatology are slightly improved in CAM3D by a westerly difference between CAM3D and CAM3 covering most of the central and southern part of China. A zone of westerly bias to the north of 40°N in CAM3 is also

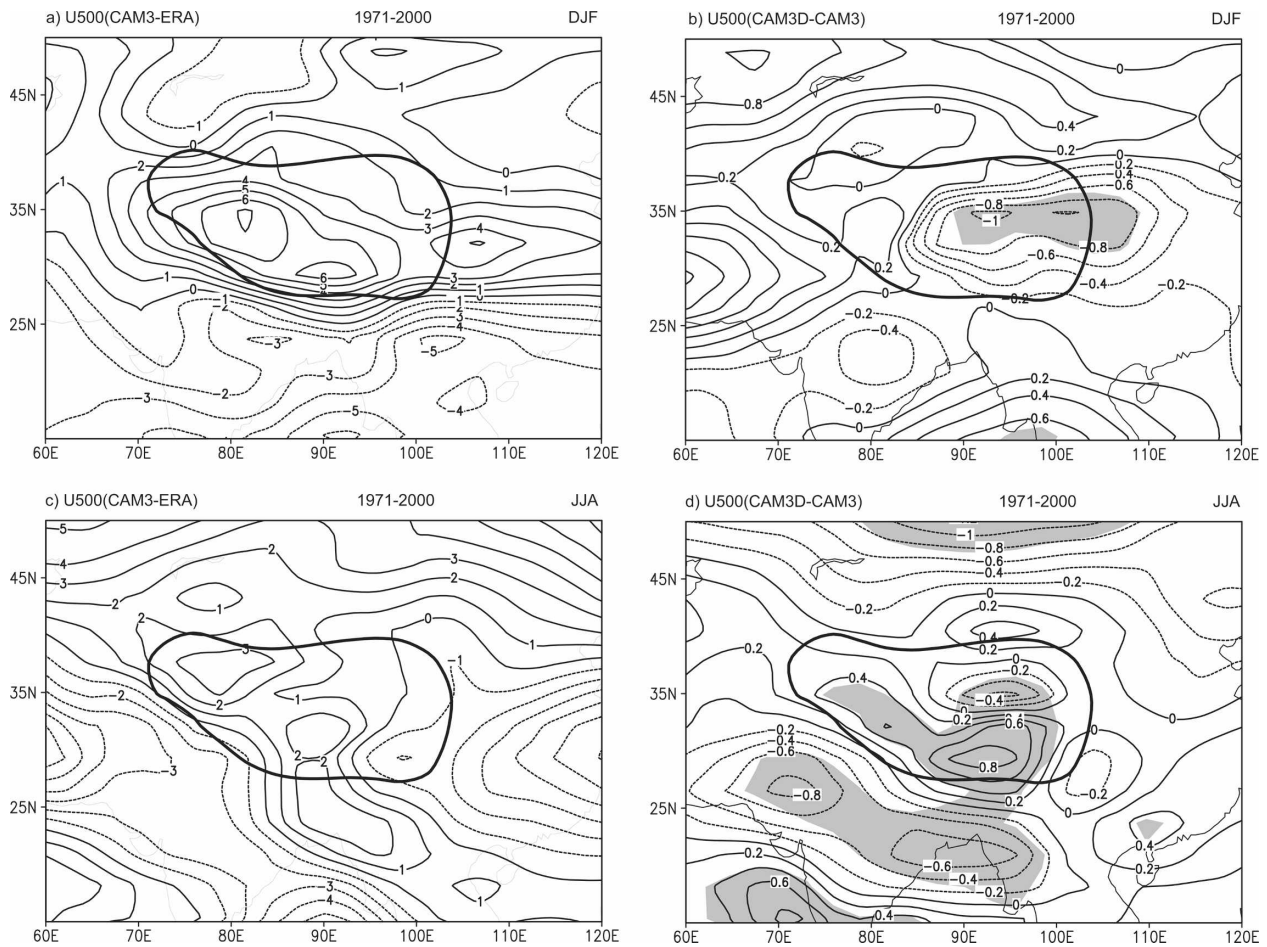


FIG. 7. As in Fig. 3 but for mean differences of zonal wind climatology at the 500-hPa level. Units are  $1 \text{ m s}^{-1}$  in (a) and (c) and  $0.2 \text{ m s}^{-1}$  in (b) and (d). The wide black lines in the center of each figure show the outline of the Tibetan Plateau at 2500 m.

reduced in CAM3D by easterly differences between CAM3D and CAM3. As during DJF, the 500-hPa wind error in CAM3 over the southwestern part of the plateau during JJA increases in CAM3D. These systematic errors in both CAM3 and CAM3D are partly related to the influence of the summer Indian monsoon and the East Asian monsoon.

Taylor diagrams (Taylor 2001) provide a statistical overview of the fields in a given region of the model in comparison with observations. The similarity between two patterns is quantified in terms of their correlation and the amplitude of their variations (represented by their standard deviations). Figure 8 presents Taylor diagrams for the distributions of 1971–2000 annual-mean climatologies over the regions of  $60^{\circ}$ – $120^{\circ}\text{E}$ ,  $10^{\circ}$ – $50^{\circ}\text{N}$  from CAM3D and CAM3 with corresponding ERA-40 reanalyses. The correlation between the model and the climatology is the cosine of the polar angle. Points lying on the dashed arc crossing “OBS” have the correct standard deviation. As shown in Fig. 8,

the geopotential height and temperature at 200 and 500 hPa, the zonal wind at 200 hPa, and the pressure at sea level from CAM3D and CAM3 generally have good agreement with observations: correlation coefficients are generally higher than 0.90 and the standard deviations in the range from 0.75 to 1.25 times the observed values. However, the zonal wind and specific humidity at 500 hPa from both the models have weak correlations with observations (correlation coefficient lower than 0.90) and have normalized standard deviations higher than 1.5. Nevertheless, the simulation levels for most variables in CAM3D, except for the zonal wind at 200 hPa and the pressure at sea level, in contrast to those in CAM3, demonstrate a slight enhancement.

## 5. Summary and discussion

In this work, we developed a complete methodology useful for spectral modeling of the atmospheric general circulation. The main point of this methodology is to introduce a stratified reference atmospheric tempera-

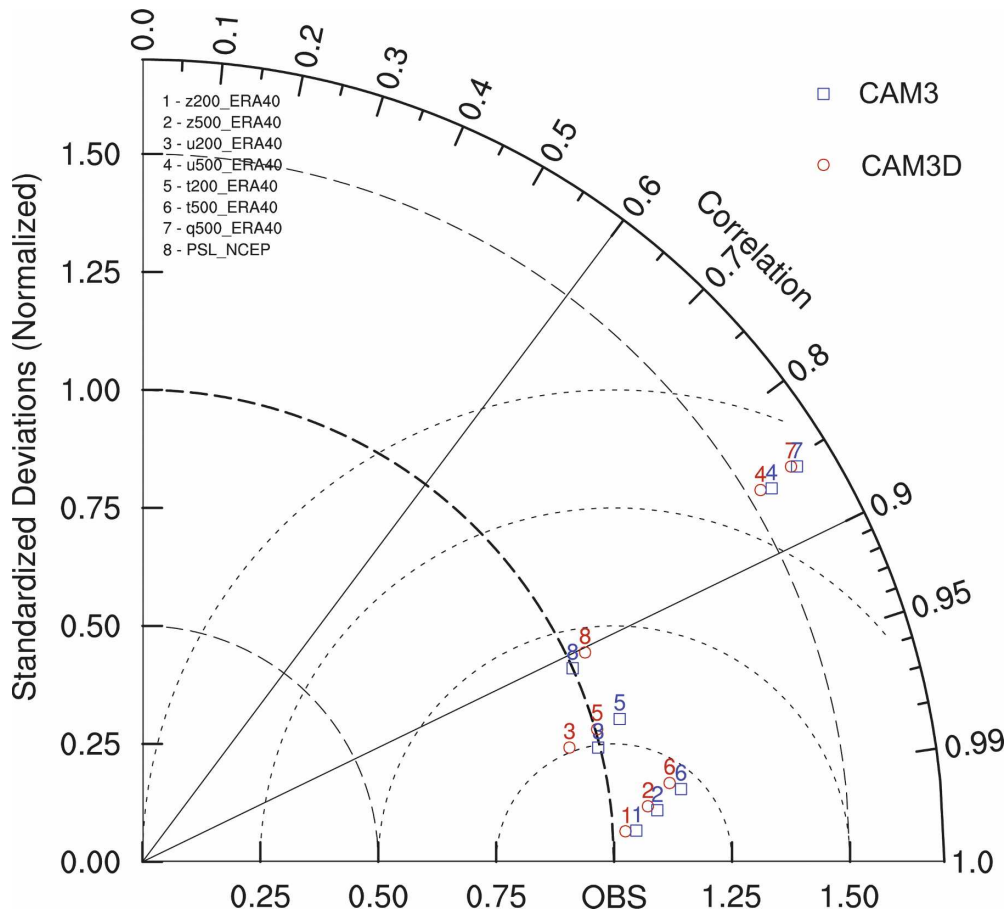


FIG. 8. Taylor diagrams summarizing the comparison of the annual mean climatology averaged for 1971–2000 over the region 10°–50°N, 60°–120°E in CAM3D and CAM3 compared with ERA-40 and NCEP reanalyses. The blue boxes and red circles show the results from CAM3 and CAM3D, respectively; *z*: geopotential height, *t*: temperature, *q*: specific humidity, and PSL: pressure at sea level; numbers refer to the pressure level of the field (hPa).

ture profile and a reference surface pressure field. By eliminating the reference state calculation from the governing equation, we are able to reduce the truncation errors in the calculation of the pressure gradient force (especially for steep topography), the temperature advection (caused by vertical discretization), and the surface pressure. The choice of the reference atmosphere is a crucial point in our approach. The reference temperature profile is close to the U.S. midlatitude standard atmosphere. The reference surface pressure is a function of surface terrain geopotential and is close to the observed surface pressure. When our methodology is implemented in a GCM, we can improve the description of the vertical structure of temperature for uneven vertical discretization and modify the calculation of pressure gradient force from a subtraction of two large terms to a sum of two small terms. We also decrease the truncation error in calculating the surface pressure and

the derivative of surface pressure with longitude and latitude.

With a simple mathematical manipulation of the original governing equations, we can demonstrate that the prognostic variables of temperature and surface pressure can be replaced by their respective perturbations from the reference values. We can furthermore deduce the corresponding prognostic equations for vorticity, divergence, perturbation temperature, and perturbation surface pressure in hybrid  $\eta$  coordinates. We developed also an explicit time difference scheme for vorticity and a semi-implicit time difference scheme for divergence, perturbation temperature, and perturbation surface pressure.

To evaluate the performance of the new dynamic framework and to compare it with the traditional dynamic framework used in atmospheric spectral modeling, we implemented this modified dynamic framework

in CAM3 in place of the normal spectral Eulerian dynamical core. The modified Eulerian dynamical model (CAM3D) and the original CAM3 are both used in simulating climates from 1971 to 2000. The two models are forced by the same underlying oceanic conditions and results are compared to the ERA-40 reanalyses. The results show a general improvement in the vertical structure of the temperature, wind, and moisture during DJF and JJA. Improvements were observed globally in almost the entire tropospheric and lower stratospheric temperature, the zonal wind between 70°S and 70°N, and the specific humidity in tropics and subtropics.

The improvement in CAM3D was also quantified using a skill score for climate models suggested by Williamson (1995). It is the normalized mean square error (NMSE) and is used for the 200-hPa height field during January in the Northern Hemisphere between 30° and 90°N, following Collins et al. (2006) and Kiehl et al. (1998). It can be separated into a sum of three nonnegative terms: one represents a measure of the unconditional bias, the second a measure of the conditional bias, and the third a measure of the phase errors. The results show that the NMSE was decreased in CAM3D with respect to CAM3, primarily in small unconditional error. A scaled variance ratio (SVR) was also calculated and it revealed that the NMSE was not artificially low due to damping of the model height field.

The effects of the modified dynamic framework on the climate over the Tibetan Plateau and its surrounding area were also demonstrated positively for the GCM. Synthetic evaluations using a Taylor diagram prove that the new dynamics implemented in CAM3D could produce improvements in the simulations of zonal wind, temperature in the lower troposphere, and sea level pressure. Remarkable improvement in the 500-hPa zonal wind occurs over the central, eastern, and northern parts of the Tibetan Plateau.

As mentioned earlier, the choice of the reference atmosphere is a crucial point of our methodology. The reference atmosphere defined in this work is distinct from that in previous similar works (e.g., Chen and Simmons 1989; Zhang et al. 1990; Simmons and Chen 1991; Sheng et al. 1992) in that it introduces a reference atmosphere into spectral models. It is worthwhile to present a short discussion on their similarities and differences. The standard stratification approximations in Chen and Simmons (1989) and Simmons and Chen (1991) are a function of pressure, posed by Zeng (1963) as following:

$$\bar{T}(p) = \frac{c_p C_0^2}{R^2} + \left( \bar{T}_0 - \frac{c_p C_0^2}{R^2} \right) \left( \frac{p}{p_0} \right)^{R/c_p}, \quad (60)$$

$$\begin{aligned} \bar{\phi}(p) = \frac{c_p}{R} + \left( R\bar{T}_0 - \frac{c_p C_0^2}{R^2} \right) \left[ 1 - \left( \frac{p}{p_0} \right)^{R/c_p} \right] \\ - \frac{c_p C_0^2}{R} \ln \left( \frac{p}{p_0} \right), \end{aligned} \quad (61)$$

where the parameter  $C_0^2$  is a constant,  $\bar{T}_0$  and  $p_0$  are the temperature and pressure at sea level, and  $\bar{T}(p)$  and  $\bar{\phi}(p)$  satisfy the hydrostatic balance equation. As shown in Fig. 1b, such a reference atmosphere fits the mean state of the atmosphere well at low levels, but not the inversion characteristics of stratification at upper levels. It is evident that there is an important difference compared to that used in our work on the stratosphere (Fig. 1a). Further sensitivity studies are underway to investigate and quantify the role of the reference atmosphere.

Zhang et al. (1990) extended the hydrostatic extraction scheme used in Chen and Simmons (1989), and Sheng et al. (1992) introduced it into BMRC's global spectral model. In their work, the temperature and geopotential height of the reference atmosphere changes with height and also with latitude as

$$\begin{aligned} \bar{T}(\varphi, p) = \frac{c_p C_0^2(\varphi, p)}{R^2} + \left[ \bar{T}_0(\varphi) - \frac{c_p C_0^2(\varphi, p)}{R^2} \right] \\ \times \left[ \frac{p}{p_0(\varphi)} \right]^{R/c_p}, \end{aligned} \quad (62)$$

$$\begin{aligned} \bar{\phi}(\varphi, p) = \frac{c_p}{R} + \left[ R\bar{T}_0(\varphi) - \frac{c_p C_0^2(\varphi, p)}{R^2} \right] \\ \times \left[ 1 - \left( \frac{p}{p_0(\varphi)} \right)^{R/c_p} \right] - \frac{c_p C_0^2(\varphi, p)}{R} \ln \left[ \frac{p}{p_0(\varphi)} \right]. \end{aligned} \quad (63)$$

Similar to the definition of (60) and (61),  $C_0^2(\varphi, p)$  is the stratification parameter describing the reference atmospheric state (calculated from the real climatology), and  $\bar{T}_0(\varphi)$  and  $p_0(\varphi)$  are the temperature and pressure at sea level. However, the assumption in Sheng et al. (1992) that the reference atmosphere does not satisfy the hydrostatic balance equation as expressed in Eq. (6) is not totally exact when used for  $\sigma$  terrain-following vertical coordinates because the parameter  $C_0^2(\mu, p)$ , which represents stratification of the reference atmosphere and changes with both height and latitude, invokes an additional nonlinear term including  $\partial C_0^2(\mu, p)/\partial p$  in the left side of Eq. (6).

In the work of Simmons and Chen (1991), the im-

provement in the spectral model for ECMWF operational medium-range prediction is tested, especially for the southern hemispheric forecasts, which indicates a small improvement over the Arctic. From this work, we find that the use of the reference atmospheric hydrostatic extraction scheme in CAM3 is also useful in improving climate simulations at regional and global scales.

However, we note that the improvement of climate performance reported throughout this paper is generally modest. This is also entirely expected as the physical parameterization, which is more responsible for the climate behaviors of a model, remains unchanged. Furthermore, the utilization of prescribed boundary conditions (SST and sea ice) exerts also a strong constraint on the model. Running the model with a fully coupled ocean may provide a more suitable framework to evaluate the performance of our methodology.

Finally, we are implementing the new dynamics into the climate system model under development at the Beijing Climate Center, China Meteorological Administration, which is intended for seasonal climate forecasting and future climate projections. Results will be reported in future papers.

*Acknowledgments.* We thank two anonymous reviewers and Dr. Laurent Z. X. Li for their constructive comments. This work was supported by the Chinese National Basic Research Program 973 (Grant 2006CB403600), the Special Program for China Meteorology Trade (Grant GYHY(QX)2007-6-5), and Chinese National Science and Technology Sustain Program (Grant 2007BAC29B00).

### APPENDIX

#### Derivation of the Time Differencing Forms for the Prognostic Equations

Equations (16), (25), and (32) may be separately rewritten as

$$\frac{\partial D}{\partial t} = -RT'_v \nabla^2 \ln p - \nabla^2 \phi' + \text{remaining nonlinear terms} \tag{A1}$$

$$\frac{\partial T'}{\partial t} = \frac{R}{c_p^*} T'_v \frac{\omega}{p} - \omega \frac{\partial \bar{T}}{\partial p} - \dot{\eta} \frac{\partial p}{\partial \eta} \frac{\partial T'}{\partial p} + \text{remaining nonlinear terms} \tag{A2}$$

$$\frac{\partial \Pi'}{\partial t} = -\frac{1}{p_s} \int_{p(\eta)}^{p(1)} D dp + \text{remaining nonlinear terms.} \tag{A3}$$

Using expressions (7) and (9),

$$\begin{aligned} -RT'_v \nabla^2 \ln p - \nabla^2 \phi' &= -RT'_v \nabla^2 \ln p - \nabla^2 \phi, \\ &= -\nabla \cdot \left( RT'_v \frac{p_s}{p} \frac{\partial p}{\partial p_s} \nabla \Pi \right) - \nabla^2 \phi_s \\ &\quad - R \int_{p(\eta)}^{p(1)} T d \ln p + \dots \end{aligned} \tag{A4}$$

With the aid of Eqs. (33), (34), and (A4), only the terms related to  $D$ ,  $T$ , and  $\Pi$  in Eqs. (A1)–(A3) are explicitly shown in the following expressions:

$$\frac{\partial D}{\partial t} = -\nabla \cdot \left( RT'_v \frac{p_s}{p} \frac{\partial p}{\partial p_s} \nabla \Pi \right) - R \int_{p(\eta)}^{p(1)} T d \ln p + \dots, \tag{A5}$$

$$\begin{aligned} \frac{\partial T'}{\partial t} &= -\left( \frac{R}{c_p} \frac{T}{p} - \frac{\partial \bar{T}}{\partial p} \right) \int_{p(\eta)}^{p(1)} D dp \\ &\quad - \left[ \frac{\partial p}{\partial p_s} \int_{p(\eta)}^{p(1)} D dp - \int_{p(\eta)}^{p(\eta)} D dp \right] \left( \frac{\partial T}{\partial p} - \frac{\partial \bar{T}}{\partial p} \right) \\ &\quad + \dots, \text{ and} \end{aligned} \tag{A6}$$

$$\frac{\partial \Pi'}{\partial t} = -\frac{1}{p_s} \int_{p(\eta)}^{p(1)} D dp + \dots. \tag{A7}$$

Now, expanding temperature and pressure about the reference state:

$$T = T^r(\eta) + (T^r)', \tag{A8}$$

$$p_s = p_s^r + (p_s^r)', \text{ and} \tag{A9}$$

$$p = p^r(\eta) + (p^r)'. \tag{A10}$$

In hybrid  $\eta$  coordinates, there is a relation:

$$d(p^r)' = (p_s^r)' d \left( \frac{\partial p^r}{\partial p_s^r} \right). \tag{A11}$$

Using the relations of (8) and (A8), one obtains

$$\begin{aligned} \nabla^2 (T^r)' &= \nabla^2 T = \nabla^2 [\bar{T}(p) + T'], \\ &= \left[ \nabla_p^2 \bar{T}(p) + \frac{\partial \bar{T}}{\partial p} \frac{\partial p}{\partial p_s} p_s \nabla^2 \Pi + \dots \right] + \nabla^2 (T'), \\ &= \frac{\partial \bar{T}}{\partial p} \frac{\partial p}{\partial p_s} p_s \nabla^2 \Pi + \nabla^2 (T') + \dots \end{aligned} \tag{A12}$$

With the aid of (A8)–(A12), expanding Eqs. (A5)–(A7) about the reference state  $T^r(\eta)$ ,  $p_s^r$ , and  $p^r(\eta)$ , and only retaining explicitly the linear terms, one obtains

$$\begin{aligned} \frac{\partial D}{\partial t} = & -RT^r \frac{p_s^r}{p^r} \frac{\partial p^r}{\partial p_s^r} \nabla^2 \Pi \\ & - R \nabla^2 \Pi \int_{p^r(\eta)}^{p^r(1)} \left[ \frac{\partial \bar{T}(p^r)}{\partial p^r} \frac{\partial p^r}{\partial p_s^r} p_s^r \right] d \ln p^r \\ & + R \int_{p^r(\eta)}^{p^r(1)} (\nabla^2 T^r) d \ln p^r + \dots, \end{aligned} \quad (\text{A13})$$

$$\begin{aligned} \frac{\partial T^r}{\partial t} = & - \left[ \frac{R T^r}{c_p p^r} - \frac{\partial \bar{T}(p^r)}{\partial p^r} \right] \int_{p^r(\eta)}^{p^r(1)} D dp^r \\ & - \left[ \frac{\partial p^r}{\partial p_s^r} \int_{p^r(\eta)}^{p^r(1)} D dp^r - \int_{p^r(\eta)}^{p^r(1)} D dp^r \right] \\ & \times \left[ \frac{\partial T^r}{\partial p^r} - \frac{\partial \bar{T}(p^r)}{\partial p^r} \right] + \dots, \end{aligned} \quad (\text{A14})$$

and

$$\frac{\partial \Pi^r}{\partial t} = - \frac{1}{p_s^r} \int_{p^r(\eta)}^{p^r(1)} D dp^r + \dots \quad (\text{A15})$$

If one defines  $GX$ ,  $GY$ , and  $GZ$  to represent the linearized terms in (A13)–(A15) respectively, the right terms of the prognostic Eqs. (16), (25), and (32) for divergence, temperature, and surface pressure can be separated into two parts, that is, nonlinear terms and linear terms, as follows:

$$\frac{\partial D}{\partial t} = (X - GX) + GX, \quad (\text{A16})$$

$$\frac{\partial T^r}{\partial t} = (Y - GY) + GY, \quad (\text{A17})$$

and

$$\frac{\partial \Pi^r}{\partial t} = (Z - GZ) + GZ, \quad (\text{A18})$$

where  $X$ ,  $Y$ , and  $Z$  represent all of the right-hand terms in Eqs. (16), (25), and (32). Then, the nonlinear terms  $(X - GX)$ ,  $(Y - GY)$ , and  $(Z - GZ)$  are treated explicitly using the value at the  $n$ th time step, and the linear terms  $GX$ ,  $GY$ , and  $GZ$  are treated implicitly by averaging the previous and next time steps. So, the semi-implicit forms of the time differencing of (A16)–(A18) may be written as

$$\frac{D^{n+1} - D^{n-1}}{2\Delta t} = X^n + \left[ \frac{GX^{n+1} + GX^{n-1}}{2} - GX^n \right], \quad (\text{A19})$$

$$\frac{(T^r)^{n+1} - (T^r)^{n-1}}{2\Delta t} = Y^n + \left( \frac{GY^{n+1} + GY^{n-1}}{2} - GY^n \right) \quad (\text{A20})$$

and

$$\frac{(\Pi^r)^{n+1} - (\Pi^r)^{n-1}}{2\Delta t} = Z^n + \left( \frac{GZ^{n+1} + GZ^{n-1}}{2} - GZ^n \right). \quad (\text{A21})$$

Expanding these and using the following relation,

$$\begin{aligned} \nabla^2 \left[ \frac{(\Pi)^{n-1} + (\Pi)^{n+1}}{2} - (\Pi)^n \right] \\ = \nabla^2 \left[ \frac{(\Pi')^{n-1} + (\Pi')^{n+1}}{2} - (\Pi')^n \right], \end{aligned} \quad (\text{A22})$$

we may obtain the expressions (37)–(39) of the time integrations for the divergence, temperature, and surface pressure.

## REFERENCES

- Arakawa, A., and M. J. Suarez, 1983: Vertical differencing of the primitive equations in sigma coordinates. *Mon. Wea. Rev.*, **111**, 34–45.
- Boer, G. J., and Coauthors, 1992: Some results from an intercomparison of the climates simulated by 14 atmospheric general circulation models. *J. Geophys. Res.*, **97**, 12 771–12 786.
- Chen, J., and A. J. Simmons, 1989: Sensitivity of medium-range weather forecasts to the use of reference atmosphere. *Adv. Atmos. Sci.*, **7**, 275–293.
- , L. Ji, and W. Wu, 1987: Design and test of an improved scheme for global spectral model with reduction truncation error. *Adv. Atmos. Sci.*, **4**, 156–168.
- Collins, W. D., and Coauthors, 2004: Description of the NCAR Community Atmosphere Model (CAM3). NCAR Tech. Note NCAR/TN-464+STR, 226 pp.
- , and Coauthors, 2006: The formulation and atmospheric simulation of the Community Atmospheric Model version 3 (CAM3). *J. Climate*, **19**, 2144–2161.
- Corby, G. A., A. Gilchrist, and R. L. Newson, 1972: A general circulation model of the atmosphere suitable for long period integrations. *Quart. J. Roy. Meteor. Soc.*, **98**, 809–832.
- Dong, M., and Coauthors, 2001: NCC atmospheric general circulation model basic principles and user's guide (in Chinese). China Meteorological Press, 152 pp.
- Gary, J. M., 1973: Estimate of truncation error in transformed coordinate primitive equation atmospheric models. *J. Atmos. Sci.*, **30**, 223–233.
- Janjić, T. Z., 1998: Comments on "A finite volume integration method for computing pressure gradient force in general vertical coordinates." *Quart. J. Roy. Meteor. Soc.*, **124**, 2527–2529.
- , and Z. I. Janjić, 1993: Spectral distributions of the pressure gradient force errors in  $\sigma$ -coordinate spectral and grid-point models in an idealized case. *Meteor. Atmos. Phys.*, **52**, 129–135.
- Janjić, Z. I., 1977: Pressure gradient force and advection scheme

- used for forecasting with steep and small scale topography. *Contrib. Atmos. Phys.*, **50**, 186–199.
- , 1989: On the pressure gradient force error in  $\sigma$ -coordinate spectral models. *Mon. Wea. Rev.*, **117**, 2285–2292.
- Johnson, D. R., and L. W. Uccellini, 1983: A comparison of methods for computing the sigma-coordinate pressure gradient force for flow over sloped terrain in a hybrid theta–sigma model. *Mon. Wea. Rev.*, **111**, 870–886.
- Kiehl, J. T., J. J. Hack, G. B. Bonan, B. B. Boville, D. L. Williamson, and P. J. Rasch, 1998: The National Center for Atmospheric Research Community Climate Model: CCM3. *J. Climate*, **11**, 1131–1149.
- Lin, S.-J., 1997: A finite volume integration method for computing pressure gradient force in general vertical coordinates. *Quart. J. Roy. Meteor. Soc.*, **123**, 1749–1762.
- , 1998: Reply to comments by T. Janjić on “A finite volume integration method for computing pressure gradient force in general vertical coordinates.” *Quart. J. Roy. Meteor. Soc.*, **124**, 2531–2533.
- Mahrer, Y., 1984: An improved numerical approximation of the horizontal pressure gradients in a terrain following coordinate system. *Mon. Wea. Rev.*, **112**, 918–922.
- Mesinger, F., and Z. I. Janjić, 1985: Problems and numerical methods of the incorporation of mountains in atmospheric models. *Lect. Appl. Math.*, **22**, 81–120.
- Michailović, D. T., and Z. I. Janjić, 1986: Comparison of methods for reducing the error of the pressure gradient force in sigma-coordinate models. *Meteor. Atmos. Phys.*, **35**, 177–184.
- Rayner, N. A., D. E. Parker, E. B. Horton, C. K. Folland, L. V. Alexander, D. P. Powell, E. C. Kent, and A. Kaplan, 2003: Global analyses of sea surface temperature, sea ice, and night marine air temperature since the late nineteenth century. *J. Geophys. Res.*, **108**, 4407, doi:10.1029/2002JD002670.
- Roeckner, E., and Coauthors, 2003: The atmospheric general circulation model ECHAM5. Part I: Model description. Max-Planck-Institut für Meteorologie Rep. 349, 127 pp.
- Sheng, H., W. Bourke, and T. Hart, 1992: An impact of hydrostatic extraction scheme on BMRC’s global spectral model. *Adv. Atmos. Sci.*, **9**, 269–278.
- Simmons, A. J., 1987: Orography and the development of the ECMWF forecast model. *Proc. ECMWF Seminar on Observation, Theory and Modelling of Orographic Effects*, Vol. 2, Reading, United Kingdom, ECMWF, 129–163.
- , and D. M. Burridge, 1981: An energy and angular-momentum conserving vertical finite-difference scheme and hybrid vertical coordinates. *Mon. Wea. Rev.*, **109**, 758–766.
- , and R. Strüfing, 1981: An energy and angular-momentum conserving finite-difference scheme, hybrid coordinates, and medium-range weather prediction. ECMWF Tech. Report 28, 68 pp.
- , and J. Chen, 1991: The calculation of geopotential and the pressure gradient in the ECMWF atmospheric model: Influence on the simulation of the polar atmosphere and on temperature analyses. *Quart. J. Roy. Meteor. Soc.*, **117**, 29–58.
- Sundqvist, H., 1975: On truncation errors in sigma-system models. *Atmosphere*, **13**, 81–95.
- , 1976: On vertical interpolation and truncation in connection with use of sigma-system models. *Atmosphere*, **14**, 37–52.
- Taylor, K. E., 2001: Summarizing multiple aspects of model performance in a single diagram. *J. Geophys. Res.*, **106**, 7183–7192.
- Williamson, D. L., 1995: Skill scores from the AMIP simulations. *Proc. First Int. AMIP Scientific Conf.*, Monterey, CA, World Meteorological Organization, 253–256.
- Wu, G., H. Liu, Y. Zhao, and W. Li, 1996: A nine-layer atmospheric general circulation model and its performance. *Adv. Atmos. Sci.*, **13**, 1–18.
- Wu, T., P. Liu, Z. Wang, Y. Liu, R. Yu, and G. Wu, 2003: The performance of atmospheric component model R42L9 of GOALS/LASG. *Adv. Atmos. Sci.*, **20**, 726–742.
- Zeng, Q., 1963: Characteristic parameter and dynamical equation of atmospheric motions (in Chinese). *Acta Meteor. Sin.*, **33**, 472–483.
- , X. Zhang, X. Liang, C. Yuan, and S. F. Chen, 1989: Documentation of IAP two-level atmospheric general circulation model. U.S. Dept. of Energy Rep. DOE/ER/60314-HI, TRO44, 383 pp.
- Zhang, D., H. Sheng, and L. Ji, 1990: Development and test of hydrostatic extraction scheme in spectral model. *Adv. Atmos. Sci.*, **7**, 142–153.